

Environmental Sensitivity of Fabry-Perot Microcavities Induced by Layered Graphene-Dielectric Hybrid Coatings

Rui Peixoto^{1,§}, J.P. Santos Pires^{1,*}, Catarina S. Monteiro^{2,3,†,§}, Maria Raposo⁴, Paulo A. Ribeiro⁴, Susana O. Silva², Orlando Frazão² and J.M. Viana Parente Lopes^{1,‡}

¹Centro de Física das Universidades do Minho e Porto and Faculty of Sciences, University of Porto, Porto 4169-007, Portugal

²Institute for Systems and Computer Engineering, Technology and Science (INESC TEC) and Department of Physics and Astronomy, Faculty of Sciences, University of Porto, Rua do Campo Alegre 687, Porto 4169-007, Portugal

³Faculty of Engineering, University of Porto, R. Dr. Roberto Frias, Porto 4200-465, Portugal

⁴Laboratory of Instrumentation, Biomedical Engineering and Radiation Physics (LIBPhys-UNL), Department of Physics, NOVA School of Science and Technology, NOVA University Lisbon, Caparica 2829-516, Portugal



(Received 2 June 2021; revised 26 August 2021; accepted 5 October 2021; published 22 October 2021)

We propose a fiber-based environmental sensor that exploits the reflection-phase-shift tunability provided by the use of layered coatings composed of dielectric slabs spaced by conducting membranes. A transfer-matrix study is done in a simplified theoretical model, for which an enhanced sensitivity of the reflection interference pattern to the output medium is demonstrated, in the typical refractive index range of liquid media. An experimental configuration using a cascaded Fabry-Perot microcavity coated by a graphene oxide/polyethylenimine (GO/PEI) multilayered structure is demonstrated. Its cost-effective chemical production method makes graphene oxide-based hybrid coatings excellent candidates for future real-life sensing devices.

DOI: [10.1103/PhysRevApplied.16.044041](https://doi.org/10.1103/PhysRevApplied.16.044041)

I. INTRODUCTION

One of the main technological applications of optical fibers is to fabricate sensing devices that can detect the tiniest changes in physical or chemical parameters. Such measurements can be very precise but are usually indirect and exploit the effect of small parametric changes in the propagation of guided light waves. The accuracy of these sensors relies on interferometry that is made possible, for instance, by building hollow-core microcavities (as small as $30\ \mu\text{m}$ [1,2]) using capillary tubes or photonic crystal fibers (PCFs) at end of a cleaved optical fiber [1,3–17], which act as miniature Fabry-Perot interferometers. Fabry-Perot cavities in optical fibers have been fabricated by Sirkis *et al.* for strain measurement [3] and, since then, similar interferometric sensors have been proposed for curvature [12], temperature [11], pressure [5], humidity [15], and acoustic sensing [17], among others. Besides, fiber-optic sensors based on Fabry-Perot interferometers have

also attracted much attention in other fields of expertise, ranging from medicine [10] to engineering [4,6].

The periodicity of the interference fringes can be made dependent on the refractive index of the environment (n_{out}). This can be achieved by endowing the output interface with a reflection phase shift that is sensitive to the wavelength (λ), an effect that can be produced by a thin coating that may feature an internal layered structure built at the nanoscale [18]. Different kinds of coatings have been used over the years, including dielectric multilayered structures [19–21], porous metal-oxide films [22], and metallic coatings based on thin metal films [23,24], plasmonic nanostructures [25] or embedded nanoparticles [26,27]. More recently, it has been reported [28] that hybrid coatings made of lossy dielectrics (transparent narrow-gap semiconductors) deposited on very thin highly conducting films can show nontrivial internal interference effects that allow for effective control over the surface reflection coefficient of light at subwavelength scales. With the advent of graphene [29,30] and other *atomically thin planar conductors* (ATPCs), it has become possible to realize similar ideas in hybrid optical coatings comprised of dielectric/ATPC/dielectric multilayered structures. In effect, if two-dimensional graphene precursors are employed, such hybrid coatings can be produced by using

*up201201453@fc.up.pt

†catarina.s.monteiro@inesctec.pt

‡jlopes@fc.up.pt

§These three authors contributed equally to the work

layer-by-layer chemical methods [31,32] that take advantage of intermolecular interactions between oppositely charged electrolytes to self-assemble a multilayered structure [33]. This inexpensive thin-film assembly has already proved to be a viable technique for real-life optical sensors of *pH* [34], oxygen detection [35], and fluorescence [36].

In this paper, we propose a fiber-based environmental sensor that consists of a Fabry-Perot microcavity coated by a hybrid structure made of dielectric polymer slabs separated by conducting two-dimensional membranes. This sensor makes use of the aforementioned nontrivial interference effects inside hybrid coatings, significantly enhancing the sensitivity of the reflection interference fringes to the output refractive index, in a range typical of liquid media. For concreteness, our theoretical analysis considers the conducting membranes to be pristine graphene sheets, the optical conductivity of which is real and roughly λ independent in the mid- to near-infrared range [37–39] (in the operational regime of the sensor). However, the precise nature of these membranes is insubstantial and the conclusions presented here only require them to be two-dimensional materials with sufficiently large real optical conductivities. Hence, more practical realizations of these devices can use hybrid optical coatings based on graphene oxide (GO) sheets [40–42], instead of actual graphene monolayers. As referred, layered structures based on these graphene precursors can be grown by inexpensive chemical processes in controlled layer-by-layer [32,33,43] procedures. Here, we employ this technique to experimentally realize the proposed sensor in a cascaded Fabry-Perot interferometer at the tip of a single-mode fiber that is coated with stacked polyethylenimine/graphene oxide (GO/PEI) layers. Such devices have recently been proposed by some of us [44] although analyzed from a different viewpoint.

The paper is organized as follows. In Sec. II, we review the optical properties of pristine graphene and highlight the similarities with existing studies on GO lattices. In Sec. III, we devise our theoretical model for the sensor, as well as the transfer-matrix formalism used to investigate the reflection properties of the hybrid dielectric/ATPC/dielectric coatings, as a function of the output refractive index and the parameters of the system. We also present the theory of interference in a low-finesse Fabry-Perot cavity, which is a key ingredient to understand the physics behind the operation of the sensor. In Sec. IV, we present our main theoretical predictions regarding the operation and performance of our idealized environmental sensor. We also point out the chief advantages of using graphene-based hybrid coatings over alternative setups. An experimental realization of this sensing device is obtained in Sec. V, including measurements that demonstrate the operation predicted by our theoretical analysis. Finally, in Sec. VI, we sum up our conclusions and speculate on future applications of this technology.

II. OPTICAL RESPONSE OF GRAPHENE AND GRAPHENE OXIDE

The crucial ingredient of this sensor is the possibility of coating the outward surface of the Fabry-Perot microcavity with a layered structure of dielectric slabs interfaced by conducting two-dimensional membranes. As explained in Sec. I, the detailed nature of these membranes is not important for our conclusions, which only depend on a dissipative optical response that is sufficiently strong but weakly dependent on the wavelength. In other words, the membrane must behave as a two-dimensional metal in the operational range of the sensor (i.e., the mid- to near-infrared spectral range). Nevertheless, the simplest, albeit paradigmatic, example of such a material is monolayer graphene, the optical response of which is concisely reviewed here. In addition, recent studies on the optical response of (more complicated) GO are also cited, highlighting the similarities with graphene that justify a direct comparison between theory and experiments in this paper.

When working around the mid- to near-infrared regime ($\lambda \gtrsim 800$ nm), it is known that the linear optical response of graphene is isotropic ($\sigma_{\lambda}^{xx} = \sigma_{\lambda}^{yy} = \sigma_{\lambda}$ are the only nonzero terms of the conductivity tensor) and that it is well described by continuum-limit calculations done within a low-energy model having two uncoupled Dirac cones [37,45,46]. More realistic modeling has also been done [47–49], which confirms this approximation as appropriate. Under this approximation, the low-temperature optical conductivity of graphene can be shown to have two contributions,

$$\sigma_{\lambda} = \sigma_{\lambda}^{\text{intra}} + \sigma_{\lambda}^{\text{inter}}, \quad (1)$$

which stem from electronic intra- and interband transitions, respectively. Both contributions can be analytically evaluated and read [45]

$$\sigma_{\lambda}^{\text{intra}} = \frac{e^2}{h} \left(\frac{2\gamma\lambda^2 |E_F|}{h^2 c^2 + \gamma^2 \lambda^2} + i \frac{2hc\lambda |E_F|}{h^2 c^2 + \gamma^2 \lambda^2} \right), \quad (2a)$$

$$\sigma_{\lambda}^{\text{inter}} = \frac{e^2}{2h} \arctan^2 \left[2 |E_F| - \frac{h}{\lambda} \gamma \right] + i \frac{e^2}{4h} \ln \left[\frac{\gamma^2 \lambda^2 + (ch - 2 |E_F| \lambda)^2}{\gamma^2 \lambda^2 + (ch + 2 |E_F| \lambda)^2} \right], \quad (2b)$$

where γ is a phenomenological scattering parameter, c is the speed of light in vacuum, h is Planck's constant, and E_F is the Fermi energy of graphene. For these approximate calculations to hold, one must always consider that $|E_F| \lesssim 0.3$ eV, corresponding to a slightly doped graphene monolayer. In Fig. 1, we show some representative plots of

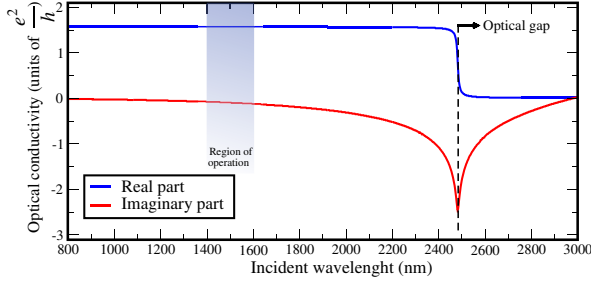


FIG. 1. Plots of the complex optical conductivity of a doped pristine graphene sheet in the infrared [see Eqs. (2a)–(2b)]. The plots consider the Fermi energy of $E_F = 0.25$ eV and a relaxation scale of $\gamma = 0.001$ eV. The optical gap and the operational regime for our sensor are indicated.

these conductivities, where it is evident that $2|E_F|$ acts as an effective “optical gap” that marks a boundary between two response regimes. For $\lambda > \pi \hbar c / |E_F|$, the dissipative interband response is suppressed by Pauli blocking and a mostly reactive current appears in the system. In contrast, for $\lambda < \pi \hbar c / |E_F|$, the imaginary part of the conductivity is almost zero and the response is mostly due to interband transitions. Then, the optical response of graphene becomes purely dissipative, with a λ -independent universal conductivity [38]. The latter is the regime where our proposed sensor will operate, such that we may take the optical conductivity to be $\sigma_\lambda \approx e^2/4\hbar$.

As noted in Sec. I, although pristine graphene could be used to realize our proposal, cheaper and more practical alternatives are provided by other two-dimensional materials, such as graphene oxide monolayers. These functionalized versions of graphene have considerably more complex structures [41] and simple expressions cannot be readily obtained for their electronic or optical response properties. However, due to the interest in graphene for optoelectronic applications [50], many *density-functional theory* (DFT) studies have been published on the linear optical properties of oxidized graphene sheets [42,51–53]. Most of the results demonstrate that, at least for moderately oxidized graphene, the optical conductivity retains a purely dissipative plateau in the midinfrared [53], with a value approximating the universal conductivity found in pristine graphene. Based on this, we argue that the theory we develop for coatings based on pristine graphene membranes also holds for GO, provided that the value of the universal optical conductivity is adjusted as a phenomenological parameter.

III. THEORETICAL MODEL FOR THE PROPOSED SENSOR

We propose a fiber-based interferometric sensor [see Fig. 2(a)] that operates on the basis of a reflection interference pattern that is sensitive to its environment. Any

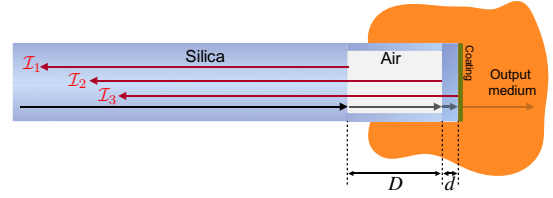


FIG. 2. The scheme of our fiber-based sensor using a three-wave micrometric Fabry-Perot cavity with an outside multilayered hybrid surface coating (shown in green) made of conducting membranes spaced by ideal dielectrics. We also define the dimensions of the Fabry-Perot microcavity (D and d) and depict the three primary waves reflected off the interfaces of the cavity (of intensity \mathcal{I}_1 , \mathcal{I}_2 and \mathcal{I}_3).

changes in the physical or chemical properties of this surrounding medium typically translate into slight alterations in its refractive index. For a bare output interface, the sensor would only be affected by variations in the absolute reflectivity of the last interface, as the phase introduced upon reflection is independent [54] of the incident wavelength. This implies that the interference pattern in the reflected spectrum is affected solely in the relative strength of its Fourier components but not in their periods. To allow a shift in the fringe periods by environmental changes, one must engineer the output interface so as to give it a λ -dependent complex reflection coefficient that also depends parametrically on the refractive index of the output medium. Such properties can be embedded into the optical interface by depositing a nanostructured coating onto the outer surface of the cavity, as described in Sec. I.

Here, we present the basic theoretical model employed to simulate the operation of our device proposal. Before proceeding with details, it is important to highlight that the sensor is naturally split into two main parts: (i) the hybrid coating on the output interface and (ii) the Fabry-Perot microcavity at the termination of the fiber. Both components work together to produce the interference effects on which the sensor is based; however, they act at different length scales. The hybrid coating is structured at the nanoscale, with typical distances of approximately 10 nm between successive conducting membranes. These lengths are shorter than optical wavelengths and thus responsible for the internal interference that causes nontrivial phase shifts upon reflection. In addition, one also has the optical interfaces forming the Fabry-Perot microcavity. These surfaces are distanced by tens or hundreds of micrometers, scales that far exceed those present in the internals of the hybrid coating. The purpose of this cavity is simply to generate a basic three-wave interference pattern in the reflected spectrum, which is then shaped by variations in the output refractive index. In the following, we consider these two main parts separately.

A. Optical modeling of a hybrid nanostructured coating

The layer-by-layer assembly method creates optical coatings where several (roughly parallel) conducting membranes are separated by nanoscopic slabs of identical dielectric material. In practice, the control over orientation, flatness, and distances between sheets is not perfect but, for modeling purposes, we consider the conducting membranes as mutually parallel planes, as shown in Fig. 3(a). Moreover, since our proposal is based on a single-mode optical fiber, it is appropriate to consider that the guided light wave has normal incidence on the coating, which simplifies the following calculations. In short, our aim is to evaluate the complex reflection and transmission coefficients of a hybrid coating featuring a given number (N) of conducting membranes spaced by a set of dielectric slabs characterized by the widths, $\{d_1, \dots, d_{N-1}\}$. This problem can be neatly solved by a *transfer-matrix method* (TMM). With no loss of generality, we consider the membranes to be pristine graphene monolayers working at the universal optical conductivity regime, i.e., $\lambda \approx 1500$ nm, while the dielectric slabs are taken as being made up of the same material (of refractive index n_{pol}).

To devise a TMM that evaluates the complex transmission (t_λ) and reflection coefficients (r_λ) of the entire coating, we begin by considering a monochromatic wave at normal incidence onto a single conducting plane [depicted in Fig. 3(b)]. In this case, both the electric and magnetic fields are parallel to the graphene sheet and the solution of the four-wave scattering problem boils down to imposing appropriate boundary conditions at the interface. Since the interface is conducting, it supports surface currents driven by the electric field of the crossing wave which, in turn, alter the usual boundary conditions associated with

a purely dielectric interface. The general electromagnetic boundary conditions in the presence of a surface conductivity are derived in Appendix A. Meanwhile, the electric field of the partial waves in Fig. 3(b) can be written as

$$\mathbf{E}^1(\mathbf{r}, t) = \left(E_\lambda^{(1,+)} e^{i\frac{2\pi n_1 z}{\lambda}} + E_\lambda^{(1,-)} e^{-i\frac{2\pi n_1 z}{\lambda}} \right) e^{i\frac{2\pi c}{\lambda} t} \hat{\mathbf{x}} \quad (3)$$

in the input medium (refractive index n_1) and

$$\mathbf{E}^2(\mathbf{r}, t) = \left(E_\lambda^{(2,+)} e^{i\frac{2\pi n_2 z}{\lambda}} + E_\lambda^{(2,-)} e^{-i\frac{2\pi n_2 z}{\lambda}} \right) e^{i\frac{2\pi c}{\lambda} t} \hat{\mathbf{x}} \quad (4)$$

in the output medium (refractive index n_2). The magnetic components of the wave are also harmonic and can be readily obtained from Faraday's law— $\mathbf{B}^{(\pm)} = \pm \hat{\mathbf{z}} \times \mathbf{E}^{(\pm)}/v_m$ —where $v_m = c/n_m$ is the speed of light in the corresponding medium. These magnetic fields read

$$\mathbf{B}^1(\mathbf{r}, t) = \left(E_\lambda^{(1,+)} e^{i\frac{2\pi n_1 z}{\lambda}} - E_\lambda^{(1,-)} e^{-i\frac{2\pi n_1 z}{\lambda}} \right) e^{i\frac{2\pi c}{\lambda} t} \frac{c}{n_1} \hat{\mathbf{y}}, \quad (5)$$

$$\mathbf{B}^2(\mathbf{r}, t) = \left(E_\lambda^{(2,+)} e^{i\frac{2\pi n_2 z}{\lambda}} - E_\lambda^{(2,-)} e^{-i\frac{2\pi n_2 z}{\lambda}} \right) e^{i\frac{2\pi c}{\lambda} t} \frac{c}{n_2} \hat{\mathbf{y}}, \quad (6)$$

with their orientation also depicted in Fig. 3(b).

Since the wave is at normal incidence, all the fields involved are parallel to the conducting interface. This leads to two important simplifications in the boundary conditions at $z = 0$: (i) only the conditions on field components parallel to the surface are of importance; and (ii) despite generating surface currents, the time-varying electric fields do not induce any superficial charge-density waves. In this case, the boundary conditions of the problem reduce to the following simpler equations:

$$\mathbf{E}_\lambda^1 = \mathbf{E}_\lambda^2, \quad (7a)$$

$$\mathbf{B}_\lambda^1 = \mathbf{B}_\lambda^2 + \mu_0 \sigma_\lambda \hat{\mathbf{z}} \times \mathbf{E}_\lambda^2, \quad (7b)$$

where $\mathbf{E}_{1/2}$ and $\mathbf{B}_{1/2}$ are the monochromatic vector amplitudes defined in Eqs. (3)–(6), σ_λ is the optical surface conductivity of the planar membrane, and μ_0 is the vacuum magnetic permeability [55]. By expressing Eqs. (7a) and (7b) in terms of only incoming or outgoing electric field amplitudes, $E_\lambda^{(1/2,\pm)}$, we cast the scattering problem in the matrix form

$$\begin{pmatrix} E_\lambda^{(2,+)} \\ E_\lambda^{(2,-)} \end{pmatrix} = \mathbb{T}_{1,2}^G(\lambda) \cdot \begin{pmatrix} E_\lambda^{(1,+)} \\ E_\lambda^{(1,-)} \end{pmatrix}, \quad (8)$$

where the transfer matrix of a single conducting interface between dielectrics of refractive indices n_1 and n_2 is

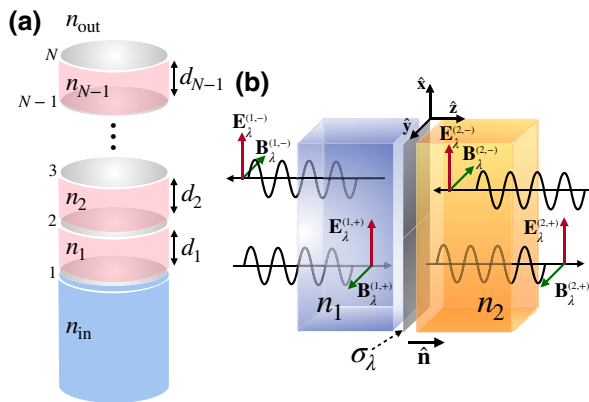


FIG. 3. (a) The toy model used to investigate the optical coefficients of the layered hybrid coating. For concreteness, we consider the conducting membranes as doped pristine graphene monolayers operating way above the optical gap. (b) The scheme of a perpendicular scattering setup for a single graphene interface between two bulk dielectrics.

given by

$$\mathbb{T}_{1,2}^G(\lambda) = \begin{pmatrix} \frac{n_2+n_1}{2n_2} - \frac{\mu_0 c \sigma_\lambda}{2n_2} & \frac{n_2-n_1}{2n_2} - \frac{\mu_0 c \sigma_\lambda}{2n_2} \\ \frac{n_2-n_1}{2n_2} + \frac{\mu_0 c \sigma_\lambda}{2n_2} & \frac{n_2+n_1}{2n_2} + \frac{\mu_0 c \sigma_\lambda}{2n_2} \end{pmatrix}. \quad (9)$$

Having the linear relation of Eq. (8), it is trivial to generalize the result and relate the input- to the output-field components in the whole structure of Fig. 3(b). For that, we recognize that a complex phase factor— $\exp(\pm i2\pi n_i d_i/\lambda)$ —is accumulated by right- and left-traveling components, respectively, when traversing the dielectric slab between layers i and $i+1$. Hence, the electric field amplitudes at the input and output media can be related as

$$\begin{pmatrix} E_\lambda^{(in,+)} \\ E_\lambda^{(in,-)} \end{pmatrix} = \mathcal{T}_\lambda \cdot \begin{pmatrix} E_\lambda^{(out,+)} \\ E_\lambda^{(out,-)} \end{pmatrix}, \quad (10)$$

where \mathcal{T}_λ is a 2×2 transfer matrix characterizing the transmission of monochromatic electromagnetic waves across the entire coating. This matrix is defined in terms of the interface matrices $\mathbb{T}_{i,i+1}^G(\lambda)$ defined in Eq. (9) and the matrices $\mathbb{P}_i = \text{diag}(\exp(i2\pi n_i d_i/\lambda), \exp(-i2\pi n_i d_i/\lambda))$ describing the phase accumulation in each dielectric slab. The general expression then reads

$$\mathcal{T}_\lambda = \mathbb{T}_{0,1}^G(\lambda) \cdot \mathbb{P}_1 \cdot \mathbb{T}_{1,2}^G(\lambda) \cdot \dots \cdot \mathbb{P}_{N-1} \cdot \mathbb{T}_{N-1,N}^G(\lambda), \quad (11)$$

where $n_0 = n_{\text{in}}$ and $n_N = n_{\text{out}}$.

Before moving on, it is worth remarking that the TMM is suitable for extremely efficient numerical evaluation, involving only successive products of very small (2×2) matrices. In our case, by specifying n_{in} , n_{out} , the list of dielectric widths $\{d_1, \dots, d_{N-1}\}$, and the corresponding refractive indices $\{n_1, \dots, n_{N-1}\}$, the transfer matrix of the whole coating can be computed in a matter of seconds on the average laptop. The complex reflection and transmission coefficients can then be extracted from its matrix elements:

$$r_\lambda = \frac{E_\lambda^{(in,-)}}{E_\lambda^{(in,+)}} = -\frac{[\mathcal{T}_\lambda]_{12}}{[\mathcal{T}_\lambda]_{22}}, \quad (12a)$$

$$t_\lambda = \frac{E_\lambda^{(out,+)}}{E_\lambda^{(in,+)}} = [\mathcal{T}_\lambda]_{11} - \frac{[\mathcal{T}_\lambda]_{12} [\mathcal{T}_\lambda]_{21}}{[\mathcal{T}_\lambda]_{22}}. \quad (12b)$$

To recap, the TMM provides a convenient and fast method to evaluate the reflection coefficient of a hybrid coating, having any number of conducting membranes with given interlayer separations and functioning at a given wavelength. Hence, in what follows, we may take r_λ as a known quantity, which one can readily evaluate for a specific case and that fully characterizes the reflection properties of the output coated surface.

B. Reflection interference pattern in a three-wave Fabry-Perot cavity

Besides the subwavelength processes within the hybrid coating, there is also interference happening at larger scales, between the waves reflected off the three interfaces that make up the low-finesse Fabry-Perot microcavity at the termination of the fiber (see the sketch in Fig. 2). Dealing with this micrometer-scale interference is not fundamentally different from our previous analysis. However, in the interest of gaining a greater insight into the operation of the sensor, we approach the problem from a different angle and approximate the reflected signal by the sum of the three primary reflections (the ones shown in Fig. 2). This approximation is justified by the low reflectivity of all the surfaces in the cavity and further confirmed by a direct comparison with the reflected spectra obtained by the TMM applied to the whole system (see Fig. 4). Considering a three-wave approximation, the intensity reflected by the microcavity is then given as

$$\begin{aligned} \mathcal{I}_r^\lambda &= \mathcal{I}_1 + \mathcal{I}_2 + \mathcal{I}_3 - 2\sqrt{\mathcal{I}_1 \mathcal{I}_2} \cos\left(\frac{4\pi D}{\lambda}\right) \\ &\quad - 2\sqrt{\mathcal{I}_2 \mathcal{I}_3} \cos\left(\frac{4\pi n_s d}{\lambda} + \theta_c^\lambda\right) \\ &\quad + 2\sqrt{\mathcal{I}_1 \mathcal{I}_3} \cos\left(\frac{4\pi(D + n_s d)}{\lambda} + \theta_c^\lambda\right), \end{aligned} \quad (13)$$

where n_s is the refractive index of the silica, d and D are the cavity widths (as defined in Fig. 2), and $\mathcal{I}_{1,2,3}$ are the intensities reflected by each interface. These intensities can be obtained from the Fresnel laws at normal incidence,

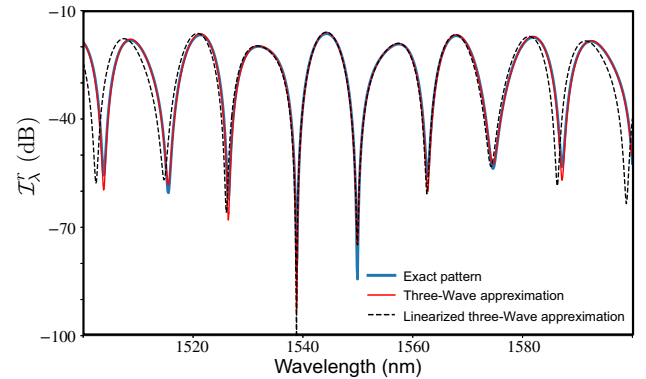


FIG. 4. The intensity reflected by the sensor as a function of the incident wavelength. The spectrum is obtained for a *simulated microcavity* ($D = 100\mu\text{ m}$ and $d = 40\mu\text{ m}$) coated by $N = 20$ graphene monolayers spaced by 20-nm dielectric slabs ($n_{\text{pol}} = 1.56$). In blue, we have the exact interference pattern, obtained from a transfer-matrix calculation on the whole system (cavity + coating), while the red and black dashed lines show the three-wave approximation [see Eq. (13)] and its linearized version [see Eq. (15)] around $\lambda_c = 1550\text{ nm}$, respectively.

reading

$$\sqrt{\mathcal{I}_1} = \left| \frac{n_s - 1}{n_s + 1} \right|, \quad \sqrt{\mathcal{I}_2} = \frac{4n_s |n_s - 1|}{(n_s + 1)^3},$$

and

$$\sqrt{\mathcal{I}_3} = \frac{16n_s^2 R_c^\lambda}{(n_s + 1)^4}. \quad (14)$$

As anticipated, effects from the output coating in the interference pattern are encapsulated in its complex reflection coefficient, specified by the corresponding reflectivity (R_c^λ) and the reflection phase shift (θ_c^λ) in all previous expressions. These parameters are crucially dependent on the incident wavelength (λ) and can be calculated by the TMM described in Sec. III. As we shall see, the λ dependence of the reflection phase shift plays a pivotal role in the operation of our sensor and is, in effect, the central concept of this paper.

Regardless of coating details, one can point out some generic features of the interference fringes. As is evident from Eq. (13), even within a three-wave approximation, a Fabry-Perot interferometer does not yield a periodic interference pattern upon reflection. Nevertheless, if only a small neighborhood of a central wavelength (λ_c) is observed, one can consider a lowest-order expansion around λ_c and a three-component periodic pattern emerges:

$$\begin{aligned} \mathcal{I}_r^{\lambda_c + \Delta\lambda} \approx & \mathcal{I}_1 + \mathcal{I}_2 + \mathcal{I}_3^{\lambda_c} \\ & - 2\sqrt{\mathcal{I}_1\mathcal{I}_2} \cos\left(\frac{2\pi\Delta\lambda}{\Lambda_1} - \frac{4\pi D}{\lambda_c^2}\right) \\ & - 2\sqrt{\mathcal{I}_2\mathcal{I}_3^{\lambda_c}} \cos\left(\frac{2\pi\Delta\lambda}{\Lambda_2} - \frac{4\pi n_s d}{\lambda_c^2} - \theta_c^{\lambda_c}\right) \\ & + 2\sqrt{\mathcal{I}_1\mathcal{I}_3^{\lambda_c}} \cos\left(\frac{2\pi\Delta\lambda}{\Lambda_3} - \frac{4\pi(D + n_s d)}{\lambda_c^2} - \theta_c^{\lambda_c}\right). \end{aligned} \quad (15)$$

This pattern features three effective periods ($\Lambda_{1,2,3}$) that arise from the interference of any combination of the three partial waves of Fig. 2. The three periods are then given as

$$\Lambda_1 = \frac{\lambda_c^2}{2D}, \quad \Lambda_2 = \frac{2\pi\lambda_c^2}{4\pi n_s d + \lambda_c^2 d\theta_c^\lambda/d\lambda|_{\lambda_c}},$$

and

$$\Lambda_3 = \frac{2\pi\lambda_c^2}{4\pi(D + n_s d) + \lambda_c^2 d\theta_c^\lambda/d\lambda|_{\lambda_c}}. \quad (16)$$

Unsurprisingly, Eq. (16) demonstrate that the effect of coating the output interface is a slight change in Λ_2 and Λ_3 , relative to their bare values. These are the components of the pattern that arise from interference with the partial wave reflected off the output interface. Interestingly, they also show that the shift in the periods is due to a λ -dependent reflection phase shift, something that would

be absent in a bare dielectric-to-dielectric interface. These shifts may increase (positive response) or decrease (negative response) the periods relative to their bare values, depending on the sign of $d\theta_c^\lambda/d\lambda|_{\lambda_c}$. As we shall see, both the sign and magnitude of this derivative can be tuned by changes in the refractive index of the output medium, thus providing the operational principle behind the sensitivity of the cavity to the environment. Note that, in practice, the individual periods of the interference pattern can be studied by band filtering the Fourier transform of the reflected signal within a narrow enough spectral window [44].

IV. NONTRIVIAL REFLECTION PHASE SHIFTS AND ENHANCED RESPONSE TO LIQUID ENVIRONMENTS

The dependence of the reflected interference fringes on the output medium is determined by the phase shifts introduced when the wave is reflected off the last interface of the microcavity. More precisely, Eq. (16) shows that a λ -dependent phase shift changes the periods in the interference pattern, with respect to their bare values (determined by the geometry of the microcavity). If the tip of the sensor is a bare dielectric-to-dielectric interface, then the reflection dephasing is independent of both λ and n_{out} . In this case, any changes to the periodicity of the fringes can only arise by geometrical alterations of the microcavity itself. However, such a situation does not hold if a thin dielectric coating (of index n_{pol} and width Δ) is placed on top of the output surface. Then, interference within the coating can bring about nontrivial phase shifts on the last partial wave, which usually depend on the wavelength. A straightforward transfer-matrix analysis of this simple setup reveals the following complex reflection coefficient:

$$r_c^\lambda = \frac{\left(\frac{n_s}{n_{\text{pol}}} - 1\right)\left(1 + \frac{n_{\text{out}}}{n_{\text{pol}}}\right) + \left(1 - \frac{n_{\text{out}}}{n_{\text{pol}}}\right)\left(1 + \frac{n_s}{n_{\text{pol}}}\right)e^{\frac{4i\pi n_{\text{pol}}\Delta}{\lambda}}}{\left(\frac{n_s}{n_{\text{pol}}} + 1\right)\left(1 + \frac{n_{\text{out}}}{n_{\text{pol}}}\right) - \left(1 - \frac{n_{\text{out}}}{n_{\text{pol}}}\right)\left(1 - \frac{n_s}{n_{\text{pol}}}\right)e^{\frac{4i\pi n_{\text{pol}}\Delta}{\lambda}}}. \quad (17)$$

From Eq. (17), one extracts the reflectivity and the reflection phase shift as functions of the incident wavelength. For our purposes, what really matters is to analyze the variation of these quantities with n_{out} , provided that the coating is nearly antireflecting (i.e., $\Delta \approx n_{\text{pol}}\lambda/2$). In Fig. 5(a), we present such an analysis for a dielectric coating ($n_{\text{pol}} = 1.6$), near antireflecting conditions, i.e., with the parameter $x = 2\Delta n_{\text{pol}}/\lambda$ valued close to 1. The main feature to be highlighted happens for an index n_{out}^* , for which the absolute reflectivity of the output surface vanishes and is accompanied by an abrupt (“resonant-like”) behavior of $d\theta_c^\lambda/d\lambda|_{\lambda_c}$. In the absence of conducting membranes, this behavior appears around $n_{\text{out}}^* = n_s$, which signals that, even for a coating with precise dimensions for destructive interference of the backscattered waves (i.e.,

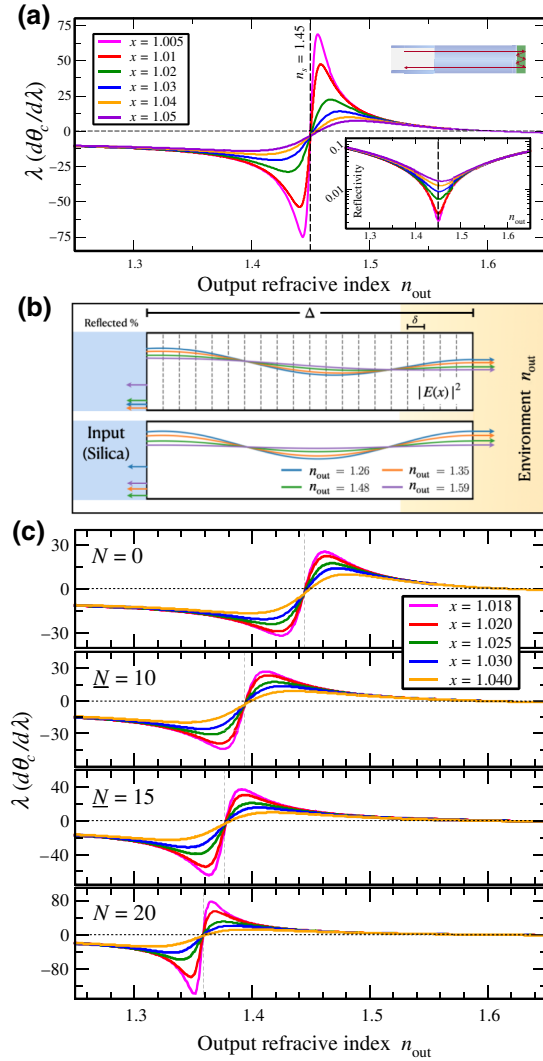


FIG. 5. (a) Simulated plots of $\lambda d\theta_c/d\lambda$ (controlling the shift of the reflected fringes) and reflectivity (in the inset), as a function of the output refractive index (n_{out}) for a purely dielectric and nearly antireflecting coating of index $n_{pol} = 1.615$ and total width $\Delta = x\lambda/2n_{pol}$. (b) The scheme of the deformed intensity profile within the coating induced by the conducting membranes. Simulated data are shown for a plain dielectric coating (bottom) and the same coating intersected by 15 graphene sheets (top). To aid visualization, the vertical axis is to be taken as proportional to the actual reflected intensity. (c) The simulated environmental dependence of $\lambda d\theta_c/d\lambda$ for hybrid coatings with $N = 0 - 20$ graphene sheets, operating at a central wavelength of $\lambda_c = 1550$ nm. The resonant response is shifted to lower n_{out} as N is increased.

$x = 1$), the interference is only partial unless the reflectivity is similar on both ends of the coating. This implies opposite discontinuities of the refractive index in the two interfaces. If the dimensions of the coating depart slightly from this $\lambda/2$ condition (or $x \approx 1$), then a nonzero reflectivity is obtained, accompanied by a broadening of the “resonantlike” response of $d\theta_c/d\lambda|_{\lambda_c}$ to n_{out} [as depicted in Fig. 5(a)].

The “resonantlike” behavior described above is of the utmost importance for this work. In fact, Eq. (16) directly implies that such a strong dependence of $d\theta_c/d\lambda|_{\lambda_c}$ on n_{out} leads to an enhanced sensitivity of the periods in the interference fringes, to the environment in which the Fabry-Perot microcavity is placed. In passing, it is also relevant to note that $d\theta_c/d\lambda|_{\lambda_c}$ increases with n_{out} in this regime, meaning that the periods of the interference fringes would have a negative environmental response. However, as the closing of the microcavity is always silica ($n_s \approx 1.45$), any purely dielectric coating would only enhance its environmental sensitivity for refractive indices $n_{out}^* \approx 1.45$, which are typical of transparent solid media. In order to operate this sensor in fluid environments, one must be able to shift this “resonantlike” behavior toward lower values of n_{out}^* . As will be demonstrated, this is the advantage of using a hybrid coating with embedded conducting membranes, instead of a dielectric one.

Inside a hybrid coating, there are conducting membranes that act as segmentations of the bulk dielectric matrix in which they lie embedded. Effectively, these membranes split the dielectric coating into chunks of average width δ , performing as conducting interfaces. The presence of these interfaces greatly affects the profile of a wave traveling inside, as they introduce additional internal reflections and also localized dissipation of field energy. The TMM devised in Sec. III takes all these effects into account and, as shown in Fig. 5(b), they lead to a nonhomogeneous field intensity that decreases along the width of the coating. This deformation of the field profile leads to a change in the condition for the absence of a reflected wave, thus requiring a larger discontinuity in the refractive index at the output boundary. As shown in Fig. 5(c), the main consequence is a down shift of n_{out}^* , which now enhances the environmental sensitivity at refractive indices within the range of 1.3 – 1.4.

Before moving on to the experimental proof of concept, it is important to recognize that the shift in n_{out}^* depends on the parameters of the coating. Namely, we show in Fig. 5(c) that n_{out}^* decreases monotonically with the number of conducting membranes, provided that the full width of the coating is kept roughly the same. Instead of looking at the resonance, the changes in n_{out}^* can be conveniently and fully characterized by tracking the reflectivity minimum. According to our previous interpretation of this “resonantlike” behavior, a minimum in the reflectivity must always accompany the resonance in $d\theta_c/d\lambda|_{\lambda_c}$. This analysis is done in Fig. 6(a) and, for low enough conductivity of the membranes, the minima depend on the coating parameters as

$$n_{out}^* = \sqrt{\frac{n_s^2 - \mu_0 c \sigma_\lambda n_s (N + 1)}{1 - \mu_0 c \sigma_\lambda n_s (N - 1) / n_{pol}^2}}, \quad (18)$$

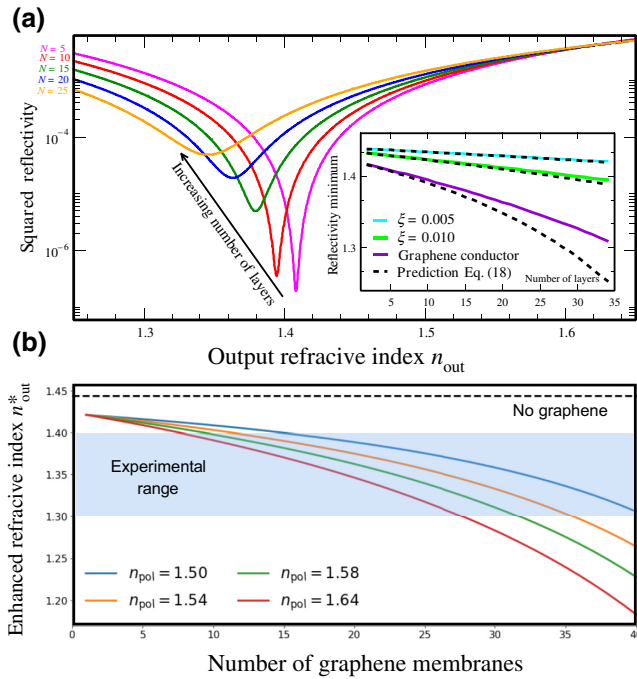


FIG. 6. (a) Plots of the reflectivity minima for simulated coatings having an increasing number of conducting membranes. The position of the minimum coincides with the index n_{out} around which the response of the sensor to environmental changes is enhanced. (b) Examples of calibration curves that show the number of graphene-dielectric bilayers needed to obtain an enhanced environmental response around a particular refractive index. The different curves refer to using different dielectric matrices in the coating and the relevant range in which to study typical liquid media is shaded in blue.

where n_s is the refractive index of silica, μ_0 is the vacuum magnetic permeability, c is the speed of light, and N is the total number of conducting membranes. Finally, this expression can be used to create approximate calibration curves [see Fig. 6(b)] that serve to guide the engineering of a coating configuration that is appropriate to enhance the environmental sensitivity around a pre-established value of the output refractive index.

V. EXPERIMENTAL DEMONSTRATION

The theoretical proposal made in previous sections is now put to the test on experimental grounds. Our prototypical device consists of a single-mode optical fiber (SMF) terminated by a cascaded Fabry-Perot microcavity interferometer (FPMI). A photograph obtained from an optical microscope is shown in Fig. 7. In order to assess the influence of an hybrid coating on the environmental sensitivity of its interference pattern, we perform a comparative study using two sensing devices: (i) an FPMI sensor coated by a single layer of bulk dielectric polymer and (ii) a similar sensor having a multilayered GO/PEI hybrid coating.

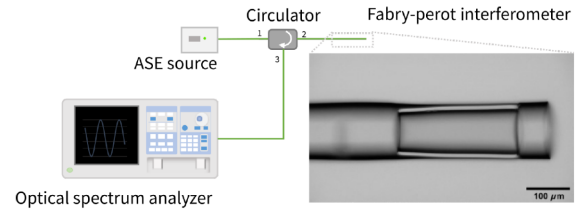


FIG. 7. The experimental setup, composed of an amplified spontaneous emission (ASE) broadband source, an optical circulator, and an optical spectral analyzer (OSA). A microscope photograph of the fabricated Fabry-Perot interferometer, with an air-cavity length of $258 \mu\text{m}$ and a silica-slab length of $64 \mu\text{m}$.

In the following, we begin by detailing technical aspects of the production method of the device and the measurement techniques. Afterward, we present experimental measurements and compare them to the predictions of our theoretical framework.

1. Fabrication of the Fabry-Perot microcavity interferometer

To build the FPMI, a silica capillary tube with an internal (external) diameter of $75 \mu\text{m}$ ($125 \mu\text{m}$) is fusion spliced (Sumitomo Type-72C) to the termination of the SMF and then cleaved to the desired length (D), using a fiber cleaver (Sumitomo FC-6RS). To close the FPMI, a second SMF is fusion spliced to the free end face of the capillary and then cleaved to a length d . The splicing processes are all carried out by using electric arcs centered far away from the capillary region. In this way, we can avoid its collapse and thus keep straight enough sides in order to minimize transverse optical losses.

2. Production of the PEI and GO/PEI coatings

For producing the optical coatings, we employ polyethylenimine (PEI) as our dielectric medium ($n_{\text{out}} = 1.615$). This polymer is acquired from Sigma-Aldrich (catalog number P3143) as a water-based solution with a 50% concentration (w/v). The PEI solution is further diluted using ultrapure water (Milli-Q water), achieving a lower concentration of 2×10^{-2} M. For producing the multilayered hybrid coatings, we use graphene oxide obtained from a commercial GO solution (Sigma-Aldrich, catalog number 777676) with a concentration of 4 mg/ml. The latter is then diluted in ultrapure water to match the same concentration of the diluted PEI solution.

All FPMIs used in this study are coated using a layer-by-layer dip coating method. For purely dielectric (PEI) coatings, the fiber is dipped into the diluted PEI solution for 1 min, followed by a brief rinse in ultrapure water to remove nonadsorbed residues. This process is repeated ten times, in order to reach a significant film thickness.

In the case of the GO/PEI coatings, a similar procedure is followed, with the FPMIs being dipped alternately into the PEI and the GO solution, with a rinse and drying step in between. Here, the repetition continues until the desired number of bilayers ($N = 10$) is attained.

3. Optical measurement setup

The experimental setup used for the characterization of the FPMIs is schematically depicted in Fig. 7. It consists of an amplified spontaneous emission (ASE) broadband source centered at $\lambda_c = 1550$ nm with a bandwidth of (approximately) 100 nm, an optical circulator, and an optical spectrum analyzer (OSA—Yokogawa AQ6370C).

A. Experimental results

The influence of coating the output surface of an FPMI is studied by comparing the reflected spectrum before and after the dip-coating process. In the presence of a PEI coating, no significant shifts or intensity changes are observed in the reflected spectrum, as obtained within an air environment. In contrast, the GO/PEI FPMI shows visible changes in the interference fringes, which appear shifted in wavelength, with a decreased intensity but a larger visibility. In Fig. 8(a), we plot the reflected signal measured before and after a sensor is coated with ten GO/PEI bilayers. The shift in the fringes is clearly marked.

Besides comparing the operation of coated and uncoated FPMIs, we focus our analysis on the influence of such coatings in their sensitivity to environmental changes. Namely, we characterize the dependence of the reflected pattern on the refractive index of the output medium by immersing the sensors in calibrated liquids, with indices ranging from $n_{\text{out}} = 1.3327$ to $n_{\text{out}} = 1.3830$ [56]. The spectra of reflected signals obtained with a GO/PEI-coated sensor are shown in Fig. 8(b), where it is evident that changing the output medium induces measurable variations in both phase and intensity of the interference fringes. No such response is obtained using a PEI-coated FPMI, as shown in Fig. 8(c), which indicates an increased environmental sensitivity of the system in the presence of a hybrid coating.

The variations in the reflected signal of the GO/PEI sensor can be more finely evaluated by performing a spectral decomposition [57] through a fast Fourier transform (FFT). The result is shown in Fig. 9(a), where the FFT amplitudes appear plotted as functions of vacuum optical-cavity lengths. From our previous theoretical analysis, it is not surprising that the FFT features exactly three peaks, associated with the three Fourier components of Eq. (15). The first peak (Λ_1), at a cavity length of $91.2 \mu\text{m}$ (corresponding to a $d = 63 \mu\text{m}$ length for $n_s = 1.4444$), is related to the optical cavity composed of fused silica and GO/PEI coating. The second peak (Λ_2), related to the air cavity, is located at a cavity length of $D = 258.3 \mu\text{m}$, while

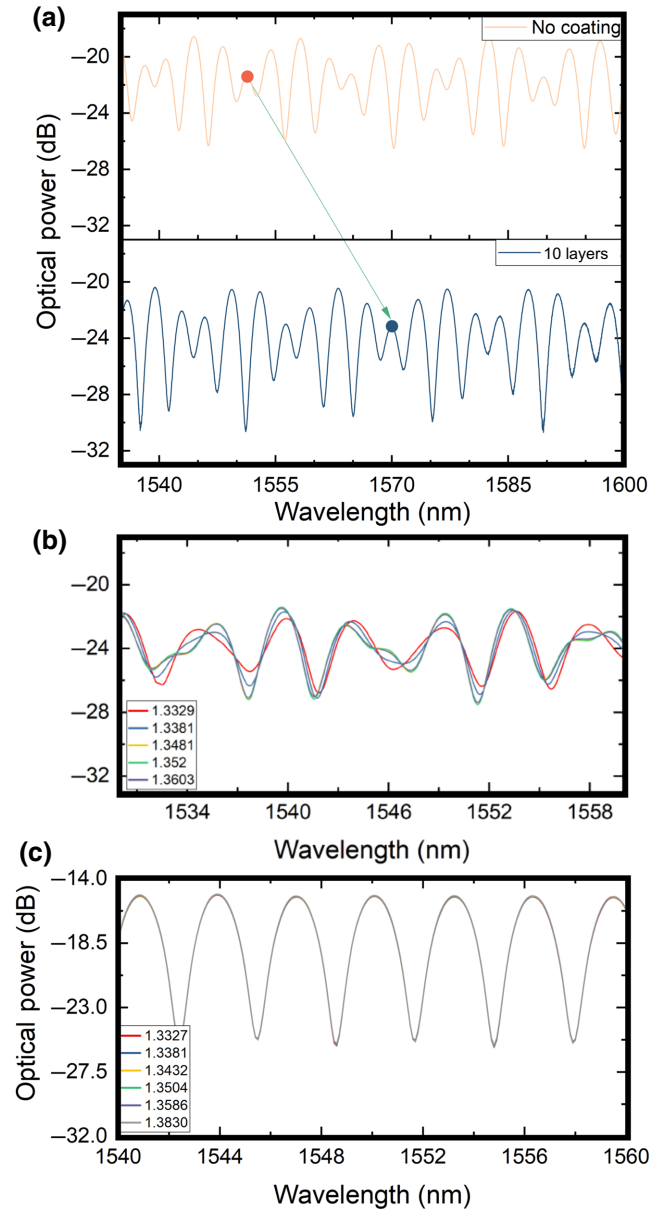


FIG. 8. (a) The measured reflected spectrum before and after the application of a coating with ten PEI/GO bilayers. The arrow makes evident the overall shift of the interference pattern (in wavelength) caused by introducing the output coating. (b) The reflected spectrum from the FPMI coated with ten PEI/GO bilayers, measured with the cavity immersed in liquid environments that have different refractive indices ($n_{\text{out}} = 1.3329 - 1.3603$). The sensitivity of the pattern is to be contrasted with (c), where an identical analysis is done using a cavity coated with PEI of roughly the same width. All the curves appear superposed.

the third peak (Λ_3) is related to the optical cavity composed of air, silica slab, and the GO/PEI coating. Note that the estimated cavity-length values are in full accordance with those determined by inspection of the microscope photograph in Fig. 7. Furthermore, small intensity variations are observed in Fig. 9(a) for the first and third peaks,

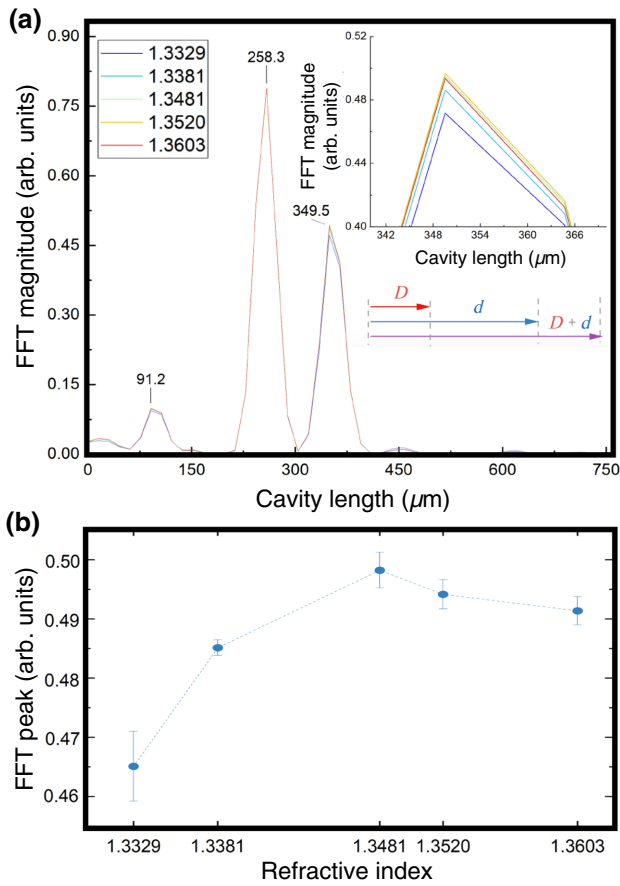


FIG. 9. (a) The Fourier transform (FFT) of the reflected spectra measured with the sensor inside the outer liquid media with varying refractive indices, coated by ten GO/PEI bilayers. (b) A study of the dependence of the intensity in the third peak on the output refractive index. The error bars are due to intrinsic spectral resolution of the OSA, which appears as random fluctuations in the measurements made over time, using the same device.

while the air-cavity peak remains unaffected by changes in the output refractive index. These results are consistent with the understanding that only Λ_1 and Λ_3 [as defined in Eq. (15)] can be affected by the reflection coefficient of the output coating and thus be sensitive to the output medium. As an example, we also plot the FFT peak intensity of Λ_3 as a function of n_{out} in Fig. 9(b).

The changes in the shape of the interference pattern depicted in Fig. 8(b) point toward an environmentally induced variation not only of the FFT peak intensities but also of their locations. Such changes in the periodicity of the pattern are consistent with our earlier theoretical predictions and therefore provide the sought-after connection between the experiments and theory presented here. In order to analyze these shifts in the Fourier components, we begin by isolating one of the sensitive peaks using a band-pass filter in the FFT. For concreteness, we

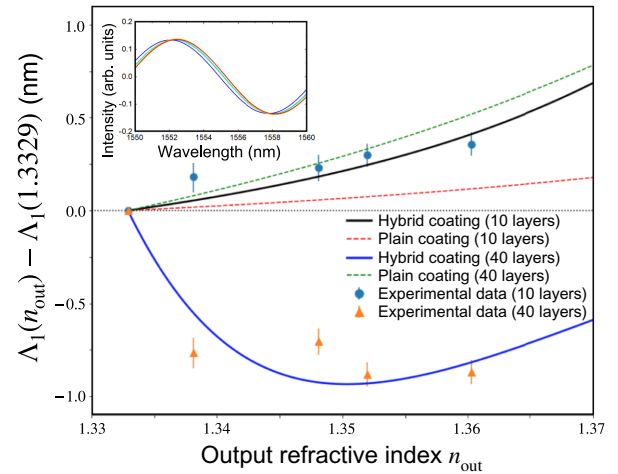


FIG. 10. The fit of the spectral shifts in the shortest period (Λ_1) measured from the filtered FFT of the reflected fringes to the theoretical model. Two data sets are shown for identical sensors coated with ten (blue points) and 40 GO/PEI bilayers (orange points). The solid lines represent the corresponding theoretical curves, obtained for reasonable values of the free parameters in the model— $\xi = 0.0188$, $n_{\text{pol}} = 1.617$ —and a distance between consecutive GO monolayers of $\delta = 95.8$ nm and $\delta = 95.6$ nm, respectively. For comparison, the corresponding curves in the absence of GO membranes (i.e., $\xi = 0$) are shown as dashed lines. The inset represents the band-filtered signal reconstructed by an inverse FFT for the coating of ten bilayers. The error bars are due to intrinsic spectral resolution of the OSA, which appears as fluctuations in the measurements made over time.

isolate the first peak (Λ_1) and obtain the filtered spectrum presented in the inset of Fig. 10. The filtered signal now exhibits an evident phase variation, which actually amounts to a shift of the period Λ_1 induced by an increase of the output refractive index. In Fig. 10, the shifts in Λ_1 are represented against our theoretical predictions for two FPMI sensors coated with $N = 10$ and $N = 40$ conducting membranes (GO) embedded into a dielectric (PEI) matrix ($n_{\text{pol}} = 1.617$ PEI [58]). Surprisingly, by using the simplified model of Sec. III and a real optical conductivity slightly smaller than pristine graphene ($\xi = 0.0188$ [59]), the agreement between the experimental data and the theoretical curves is reasonably good for both cases. The average distance between consecutive GO sheets is slightly adjusted for the fit ($\delta = 95.8$ nm and $\delta = 95.6$ nm, respectively) but the values are close enough to indicate good consistency in the production of the multilayered coating. Given the imperfections expected to be present in a GO/PEI coating produced using a chemical layer-by-layer technique, we can argue that our experimental results are consistent with the down shift of a “resonantlike” behavior in the reflection phase shift at the output surface of the FPMI, as theoretically predicted for hybrid coatings in Sec. IV.

VI. CONCLUSIONS AND OUTLOOK

We propose and experimentally demonstrate an interferometric sensor, based on a Fabry-Perot microcavity built at the end of a single-mode optical fiber and covered by a thin multilayered hybrid coating made of two-dimensional (graphenelike) conducting membranes embedded within a dielectric matrix. Unlike more conventional Fabry-Perot sensors, the proposed device is able to sense changes in the refractive index of the output medium by translating them to measurable shifts in the Fourier periods that compose the reflected spectrum. Our theoretical study shows that the aforementioned changes in the interference pattern can be attributed to an enhanced environmental sensitivity of the reflection phase shift introduced by the output coating. The latter is caused by complex internal reflection, interference, and energy-loss processes among the different conducting surfaces contained within the coating. Moreover, as the number of layers in the coating increases, the sensitivity is enhanced for lower values of the output refractive index, which allows the engineering of a sensor that works within range of indices typically found on liquid media ($n_{\text{out}} \approx 1.3 - 1.4$). The theoretical predictions are further tested against reflected spectral measurements done on an experimental realization of this device that employs GO/PEI multilayered structures produced using a cost-effective layer-by-layer chemical dip-coating process. Despite inherent imperfections in the structure of the coating and the possible influence of other external physical parameters (e.g., thermal sensitivity), sensible agreement is obtained between the measurements and the theoretical predictions. Besides demonstrating the concept, this agreement further encourages investment in these types of devices for future real-life sensing applications.

As a closing remark, we comment on the technological applicability of the sensing devices described in this work. In reality, for these hybrid coatings to be of practical use, a more consistent production method that creates more resilient and/or durable hybrid coatings is imperative. In particular, the interference phenomenon described here is very sensitive to imperfections in the layered structure, namely the film roughness shown in Fig. 11. This roughness is a typical feature known to occur in polymeric films produced using layer-by-layer techniques [60–62] and can

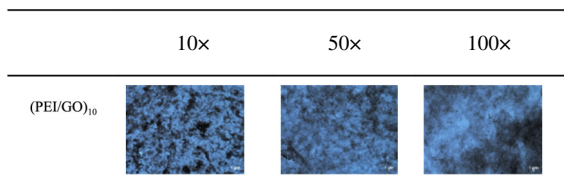


FIG. 11. Optical-microscopy images of a film of ten GO/PEI bilayers deposited on glass. The roughness of the polymeric film is clear from the picture.

eventually be controlled. Surely, the use of vapor-phase deposition techniques could potentially allow more perfectly structured coatings to be made. However, such methods would be highly inefficient, and likely more expensive, ways to produce these multilayered coatings. Nevertheless, the basic concepts underlying the operation of these hybrid coatings are arguably more general than our current experimental realization and this work could serve as a spark for future technological developments.

ACKNOWLEDGMENTS

We acknowledge financial support by the Portuguese Foundation for Science and Technology (FCT) within the Strategic Funding (Grant No. UIDB/04650/2020) and COMPETE 2020 program in the FEDER component (European Union), through Grant No. POCI-01-0145-FEDER-028887 and UltraGraf (Grant No. M-ERA-NET2/0002/2016). J.P.S.P. and C.S.M. were further supported by FCT Ph.D. Grants No. PD/BD/142774/2018 and No. SFRH/BD/135820/2018, respectively. J.P.S.P. thanks S. M. João, C. D. Fernandes, Professor J. M. B. Lopes dos Santos, and Professor N. M. R. Peres for profitable discussions and useful comments on this work.

APPENDIX: ELECTRODYNAMIC BOUNDARY CONDITIONS IN CONDUCTING INTERFACES

The existence of sharp interfaces separating different dielectric media is known to introduce discontinuities in components of electric and/or magnetic fields. In the simplest case, these interfaces are electrically neutral and cannot support charge currents. For this work, however, we must consider cases in which this last condition does not hold, because the interfaces are two-dimensional conducting membranes (e.g., graphene monolayers). In this appendix, we derive the general boundary conditions for such a planar interface, assuming that the two dielectrics have refractive indices n_1 and n_2 , while the interface is a linear conducting membrane described by a complex conductivity $\sigma_\lambda = \sigma'_\lambda + i\sigma''_\lambda$.

To obtain these boundary conditions, we begin by considering the interface to be planar. Despite not involving loss of generality, this geometrical arrangement allows the construction of the usual pillbox Gauss surface [Fig. 12(a)] and Ampère square circuit [Fig. 12(b)] that allow us to apply Maxwell's equations in integral form:

$$\oiint_{S_V} \mathbf{D}(\mathbf{r}, t) \cdot d\mathbf{S} = \iiint_V \rho(\mathbf{r}, t) d\mathbf{r}, \quad (\text{A1a})$$

$$\oiint_{S_V} \mathbf{B}(\mathbf{r}, t) \cdot d\mathbf{S} = 0, \quad (\text{A1b})$$

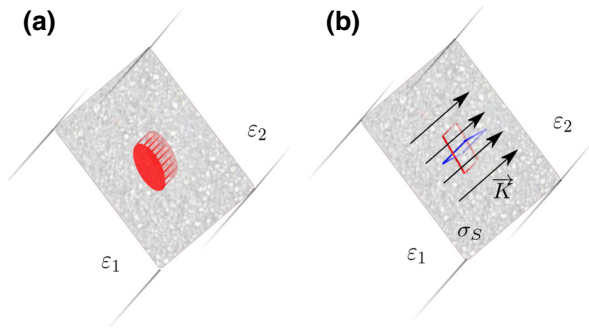


FIG. 12. (a) A pillbox surface traversing the interface between the two dielectric media. (b) The square circuit used to derive the boundary conditions for the parallel components.

$$\oint_C \mathbf{E}(\mathbf{r}, t) \cdot d\mathbf{S} = -\iint_{S_C} \left[\frac{\partial}{\partial t} \mathbf{B}(\mathbf{r}, t) \right] \cdot d\mathbf{S}, \quad (\text{A1c})$$

$$\begin{aligned} \oint_C \mathbf{B}(\mathbf{r}, t) \cdot d\mathbf{S} &= \mu_0 \iint_{S_C} \mathbf{J}(\mathbf{r}, t) \cdot d\mathbf{S} \\ &\quad - \mu_0 \iint_{S_C} \left[\frac{\partial}{\partial t} \mathbf{D}(\mathbf{r}, t) \right] \cdot d\mathbf{S}, \end{aligned} \quad (\text{A1d})$$

where \mathbf{E} , \mathbf{B} , and \mathbf{D} are the electric, magnetic, and electric displacement fields, respectively. In order to keep the discussion as focused as possible, we assume that all these fields are harmonic in space-time, e.g., $\mathbf{E}(\mathbf{r}, t) = \mathbf{E}_0 \exp(i\mathbf{k} \cdot \mathbf{r} - i\omega t)$, and that the interface is aligned with the plane $z = 0$. Assuming an wavelength $\lambda = 2\pi/|\mathbf{k}|$, the Ohmic surface currents at the interfaces are simply

$$\mathbf{K}(\mathbf{r}, t) = \mathbf{K}_0 \exp(i\mathbf{k} \cdot \mathbf{r} - i\omega t), \quad (\text{A2})$$

where $\mathbf{K}_0 = \sigma_\lambda \mathbf{E}_0^\parallel$. Hereafter, we use \parallel (\perp) to represent vectors that are parallel (perpendicular) to the interface. Since the current of Eq. (A2) is time dependent, the condition of local current conservation implies that a time-dependent change-density wave is also usually generated. The latter can be obtained from the two-dimensional continuity equation,

$$\frac{\partial \rho_s(\mathbf{r}, t)}{\partial t} = \nabla_{xy} \mathbf{K}(\mathbf{r}, t), \quad (\text{A3})$$

which yields $\rho_s(\mathbf{r}, t) = \rho_s^0 \exp(i\mathbf{k}^\perp \cdot \mathbf{r} - i\omega t)$, where

$$\rho_s^0 = \frac{\sigma_\lambda}{\omega} \mathbf{E}_0^\parallel \cdot \mathbf{k}. \quad (\text{A4})$$

If we now use the surface current and charge densities of Eqs. (A2) and (A4) and apply the integral Maxwell's

equations to the constructions of Fig. 12, we obtain the following general conditions for the fields in the two sides of the planar interface:

$$\mathbf{E}_{0,1}^\parallel = \mathbf{E}_{0,2}^\parallel, \quad (\text{A5a})$$

$$\varepsilon_1 \mathbf{E}_{0,1}^\perp = \varepsilon_2 \mathbf{E}_{0,2}^\perp + \frac{\sigma_\lambda}{\omega} \mathbf{E}_{0,1}^\parallel \cdot \mathbf{k}, \quad (\text{A5b})$$

$$\mathbf{B}_{0,1}^\perp = \mathbf{B}_{0,2}^\perp, \quad (\text{A5c})$$

$$\mathbf{B}_1^\parallel = \mathbf{B}_2^\parallel + \mu_0 \sigma_\lambda \hat{\mathbf{n}} \times \mathbf{E}_{0,1}^\parallel, \quad (\text{A5d})$$

where ε_1 are the dielectric constants of the two media. Finally, if we consider the case of perpendicular incidence, then the perpendicular components are zero and $\hat{\mathbf{n}} \times \mathbf{E}_{0,1}^\parallel = \mathbf{E}_{0,1}$. In this way, we recover the special case quoted in Eqs. (7a)–(7b).

-
- [1] C.-L. Lee, H.-Y. Ho, J.-H. Gu, T.-Y. Yeh, and C.-H. Tseng, Dual hollow core fiber-based Fabry-Perot interferometer for measuring the thermo-optic coefficients of liquids, *Opt. Lett.* **40**, 459 (2015).
 - [2] A. D. Gomes, M. Becker, J. Dellith, M. I. Zibaii, H. Latifi, M. Rothhardt, H. Bartelt, and O. Frazão, Multimode Fabry-Perot interferometer probe based on Vernier effect for enhanced temperature sensing, *Sensors* **19**, 453 (2019).
 - [3] J. S. Sirkis, D. D. Brennan, M. A. Putman, T. A. Berkoff, A. D. Kersey, and E. J. Friebele, In-line fiber étalon for strain measurement, *Opt. Lett.* **18**, 1973 (1993).
 - [4] B. Yu, D. W. Kim, J. Deng, H. Xiao, and A. Wang, Fiber Fabry-Perot sensors for detection of partial discharges in power transformers, *Appl. Opt.* **42**, 3241 (2003).
 - [5] X. Wang, J. Xu, Y. Zhu, K. L. Cooper, and A. Wang, All-fused-silica miniature optical fiber tip pressure sensor, *Opt. Lett.* **31**, 885 (2006).
 - [6] W. R. Habel and K. Krebber, Fiber-optic sensor applications in civil and geotechnical engineering, *Photonic Sensors* **1**, 268 (2011).
 - [7] D. J. J. Hu, Y. Wang, J. L. Lim, T. Zhang, K. B. Milenko, Z. Chen, M. Jiang, G. Wang, F. Luan, P. P. Shum, Q. Sun, H. Wei, W. Tong, and T. R. Wolinski, Novel miniaturized Fabry-Perot refractometer based on a simplified hollow-core fiber with a hollow silica sphere tip, *IEEE Sens. J.* **12**, 1239 (2012).
 - [8] F. C. Favero, L. Araujo, G. Bouwmans, V. Finazzi, J. Villatoro, and V. Pruneri, Spheroidal Fabry-Perot microcavities in optical fibers for high-sensitivity sensing, *Opt. Express* **20**, 7112 (2012).
 - [9] D. Jáuregui-Vázquez, J. M. Estudillo-Ayala, R. Rojas-Laguna, E. Vargas-Rodríguez, J. M. Sierra-Hernández, J. C. Hernández-García, and R. I. Mata-Chávez, An all fiber intrinsic Fabry-Perot interferometer based on an air-microcavity, *Sensors* **13**, 6355 (2013).

- [10] X. Zou, N. Wu, Y. Tian, J. Ouyang, K. Barringhaus, and X. Wang, Miniature Fabry-Perot fiber optic sensor for intravascular blood temperature measurements, *IEEE Sens. J.* **13**, 2155 (2013).
- [11] M. S. Ferreira, P. Roriz, J. Bierlich, J. Kobelke, K. Wondraczek, C. Aichele, K. Schuster, J. L. Santos, and O. Frazão, Fabry-Perot cavity based on silica tube for strain sensing at high temperatures, *Opt. Express* **23**, 16063 (2015).
- [12] C. S. Monteiro, M. S. Ferreira, S. O. Silva, J. Kobelke, K. Schuster, J. Bierlich, and O. Frazão, Fiber Fabry-Perot interferometer for curvature sensing, *Photonic Sensors* **6**, 339 (2016).
- [13] L. Yan, Z. Gui, G. Wang, Y. An, J. Gu, M. Zhang, X. Liu, Z. Wang, G. Wang, and P. Jia, A micro bubble structure based Fabry-Perot optical fiber strain sensor with high sensitivity and low-cost characteristics, *Sensors* **17**, 555 (2017).
- [14] A. D. Gomes, C. S. Monteiro, B. Silveira, and O. Frazão, A brief review of new fiber microsphere geometries, *Fibers* **6**, 48 (2018).
- [15] B. Wang, J. Tian, L. Hu, and Y. Yao, High sensitivity humidity fiber-optic sensor based on all-agar Fabry-Perot interferometer, *IEEE Sens. J.* **18**, 4879 (2018).
- [16] C. S. Monteiro, J. Kobelke, K. Schuster, J. Bierlich, S. O. Silva, and O. Frazão, High sensitivity strain sensor based on twin hollow microspheres, *Microw. Opt. Technol. Lett.* **61**, 454 (2019).
- [17] C. S. Monteiro, M. Raposo, P. A. Ribeiro, S. O. Silva, and O. Frazão, Acoustic optical fiber sensor based on graphene oxide membrane, *Sensors* **21**, 2336 (2021).
- [18] P. Baumeister, *Optical Coating Technology*, SPIE Press Monograph (SPIE Optical Engineering Press, Bellingham, Washington, 2004).
- [19] P. M. Martin, D. C. Stewart, W. D. Bennett, J. D. Affinito, and M. E. Gross, Multifunctional multilayer optical coatings, *J. Vac. Sci. Technol. A* **15**, 1098 (1997).
- [20] K. Jiang, A. Zakutayev, J. Stowers, M. D. Anderson, J. Tate, D. H. McIntyre, D. C. Johnson, and D. A. Keszler, Low-temperature, solution processing of TiO₂ thin films and fabrication of multilayer dielectric optical elements, *Solid State Sci.* **11**, 1692 (2009).
- [21] P. Yeh, *Optical Waves in Layered Media*, Wiley Series in Pure and Applied Optics (John Wiley & Sons, Hoboken, New Jersey, 2005).
- [22] B. E. Yoldas, Investigations of porous oxides as an antireflective coating for glass surfaces, *Appl. Opt.* **19**, 1425 (1980).
- [23] L.-P. Sung, M. E. Nadal, M. E. McKnight, E. Marx, and B. Laurenti, Optical reflectance of metallic coatings: Effect of aluminum flake orientation, *J. Coat. Technol.* **74**, 55 (2002).
- [24] H. Chen, H. Fu, X. Huang, Z. Lu, X. Zhang, J. Montes, and Y. Zhao, Optical cavity effects in InGaN micro-light-emitting diodes with metallic coating, *IEEE Photonics J.* **9**, 1 (2017).
- [25] V. G. Kravets, F. Schedin, and A. N. Grigorenko, Plasmonic blackbody: Almost complete absorption of light in nanostructured metallic coatings, *Phys. Rev. B* **78**, 205405 (2008).
- [26] K. C. Krogman, T. Druffel, and M. K. Sunkara, Anti-reflective optical coatings incorporating nanoparticles, *Nanotechnology* **16**, S338 (2005).
- [27] D. J. Choi, J. S. Maeng, K.-o. Ahn, M. J. Jung, S. H. Song, and Y.-H. Kim, Synthesis of Cu or Cu₂O-polyimide nanocomposites using Cu powders and their optical properties, *Nanotechnology* **25**, 375604 (2014).
- [28] M. A. Kats, R. Blanchard, P. Genevet, and F. Capasso, Nanometre optical coatings based on strong interference effects in highly absorbing media, *Nat. Mater.* **12**, 20 (2013).
- [29] K. S. Novoselov, A. K. Geim, S. V. Morozov, D. Jiang, Y. Zhang, S. V. Dubonos, I. V. Grigorieva, and A. A. Firsov, Electric field effect in atomically thin carbon films, *Science* **306**, 666 (2004).
- [30] A. K. Geim and K. S. Novoselov, The rise of graphene, *Nat. Mater.* **6**, 183 (2007).
- [31] M. Keeney, X. Y. Jiang, M. Yamane, M. Lee, S. Goodman, and F. Yang, Nanocoating for biomolecule delivery using layer-by-layer self-assembly, *J. Mater. Chem. B* **3**, 8757 (2015).
- [32] M. Björnalm, J. Cui, N. Bertleff-Zieschang, D. Song, M. Faria, M. A. Rahim, and F. Caruso, Nanoengineering particles through template assembly, *Chem. Mater.* **29**, 289 (2017).
- [33] N. I. Kovtyukhova, P. J. Ollivier, B. R. Martin, T. E. Mal-louk, S. A. Chizhik, E. V. Buzaneva, and A. D. Gorchinskiy, Layer-by-layer assembly of ultrathin composite films from micron-sized graphite oxide sheets and polycations, *Chem. Mater.* **11**, 771 (1999).
- [34] J. Goicoechea, C. R. Zamarreño, I. R. Matías, and F. J. Arregui, Optical fiber pH sensors based on layer-by-layer electrostatic self-assembled neutral red, *Sens. Actuators B: Chem.* **132**, 305 (2008).
- [35] C. Elosua, N. de Acha, M. Hernaez, I. R. Matias, and F. J. Arregui, Layer-by-layer assembly of a water-insoluble platinum complex for optical fiber oxygen sensors, *Sens. Actuators B: Chem.* **207**, 683 (2015).
- [36] H. M. R. Gonçalves, A. J. Duarte, F. Davis, S. P. J. Higson, and J. C. G. Esteves da Silva, Layer-by-layer immobilization of carbon dots fluorescent nanomaterials on single optical fiber, *Anal. Chim. Acta.* **735**, 90 (2012).
- [37] T. Stauber, N. M. R. Peres, and A. K. Geim, Optical conductivity of graphene in the visible region of the spectrum, *Phys. Rev. B* **78**, 085432 (2008).
- [38] R. R. Nair, P. Blake, A. N. Grigorenko, K. S. Novoselov, T. J. Booth, T. Stauber, N. M. R. Peres, and A. K. Geim, Fine structure constant defines visual transparency of graphene, *Science* **320**, 1308 (2008).
- [39] N. M. R. Peres, Colloquium: The transport properties of graphene: An introduction, *Rev. Mod. Phys.* **82**, 2673 (2010).
- [40] W. S. Hummers and R. E. Offeman, Preparation of graphitic oxide, *J. Am. Chem. Soc.* **80**, 1339 (1958).
- [41] K. A. Mkhoyan, A. W. Contryman, J. Silcox, D. A. Stewart, G. Eda, C. Mattevi, S. Miller, and M. Chhowalla, Atomic and electronic structure of graphene-oxide, *Nano Lett.* **9**, 1058 (2009).
- [42] S. Schöche, N. Hong, M. Khorasaninejad, A. Ambrosio, E. Orabona, P. Maddalena, and F. Capasso, Optical properties of graphene oxide and reduced graphene oxide determined by spectroscopic ellipsometry, *Appl. Surf. Sci.* **421**, 778 (2017).

- [43] J. J. Richardson, J. Cui, M. Björnmalm, J. A. Braunger, H. Ejima, and F. Caruso, Innovation in layer-by-layer assembly, *Chem. Rev.* **116**, 14828 (2016).
- [44] C. S. Monteiro, M. Raposo, P. A. Ribeiro, S. O. Silva, and O. Frazão, Tuning of fiber optic surface reflectivity through graphene oxide-based layer-by-layer film coatings, *Photonics* **7**, 11 (2020).
- [45] S. A. Mikhailov, Quantum theory of the third-order nonlinear electrodynamic effects of graphene, *Phys. Rev. B* **93**, 085403 (2016).
- [46] G. B. Ventura, D. J. Passos, J. M. B. Lopes dos Santos, J. M. Viana Parente Lopes, and N. M. R. Peres, Gauge covariances and nonlinear optical responses, *Phys. Rev. B* **96**, 035431 (2017).
- [47] T. P. Cysne, T. G. Rappoport, A. Ferreira, J. M. Viana Parente Lopes, and N. M. R. Peres, Numerical calculation of the Casimir-Polder interaction between a graphene sheet with vacancies and an atom, *Phys. Rev. B* **94**, 235405 (2016).
- [48] S. M. João and J. M. Viana Parente Lopes, Basis-independent spectral methods for non-linear optical response in arbitrary tight-binding models, *J. Phys.: Cond. Matt.* **32**, 125901 (2019).
- [49] S. M. João, M. Andelkovic, L. Covaci, T. G. Rappoport, J. M. Viana Parente Lopes, and A. Ferreira, KITE: High-performance accurate modelling of electronic structure and response functions of large molecules, disordered crystals and heterostructures, *Royal Soc. Open Sci.* **7**, 191809 (2020).
- [50] X.-M. Huang, L.-Z. Liu, S. Zhou, and J.-J. Zhao, Physical properties and device applications of graphene oxide, *Front. Phys.* **15**, 33301 (2020).
- [51] H. Huang, Z. Li, J. She, and W. Wang, Oxygen density dependent band gap of reduced graphene oxide, *J. Appl. Phys.* **111**, 054317 (2012).
- [52] F. Nasehnia and M. Seifi, Optical conductivity of partially oxidized graphene from first principles, *J. Appl. Phys.* **118**, 014304 (2015).
- [53] F. Nasehnia, S. Mohammadpour Lima, M. Seifi, and E. Mehran, First principles study on optical response of graphene oxides: From reduced graphene oxide to the fully oxidized surface, *Comput. Mater. Sci.* **114**, 112 (2016).
- [54] In these conditions, it can only change from 0 to π if the output refractive index (n_{out}) exceeds that of silica.
- [55] We always assume the magnetic effects to be irrelevant for the optical properties of our system.
- [56] These indices are determined using an Abbe refractometer (Atago DR-A1), with a light source with a wavelength approximately equal to that of the sodium *D* line (589.3 nm).
- [57] The FFT is calculated after converting the dB-reflected signal into linear optical power.
- [58] Refractiveindex.info, accessed: 2021-06-02.
- [59] As opposed to $\xi \approx 0.0229$ for pristine graphene sheets working in the mid- to near-infrared regime.
- [60] Q. Ferreira, P. J. Gomes, Y. Nunes, M. J. P. Maneira, P. A. Ribeiro, and M. Raposo, Atomic force microscope characterization of PAH/PAZO multilayers, *Microelectron. Eng.* **84**, 506 (2007).
- [61] A. A. Duarte, S. L. Filipe, L. M. Abegão, P. J. Gomes, P. A. Ribeiro, and M. Raposo, Adsorption kinetics of DPPG liposome layers: A quantitative analysis of surface roughness, *Microsc. Microanal.* **19**, 867 (2013).
- [62] M. Raposo, Q. Ferreira, A. R. Monteiro Timóteo, P. A. Ribeiro, and A. M. B. do Rego, Contribution of counterions and degree of ionization for birefringence creation and relaxation kinetics parameters of PAH/PAZO films, *J. Appl. Phys.* **118**, 114504 (2015).